An optical technique for the measurement of longshore currents

C. C. Chickadel, R. A. Holman, and M. H. Freilich
College of Oceanic and Atmospheric Sciences, Oregon State University, Corvallis, Oregon, USA

Received 9 January 2003; revised 18 August 2003; accepted 23 September 2003; published 26 November 2003.

[1] We present an optical method (optical current meter) to measure the longshore component of nearshore surface currents by measuring the alongshore drift of persistent sea foam in the surf zone. The method uses short time series of video data collected from an alongshore array of pixels. These space-time data are first Fourier transformed to a frequency-wave number spectrum and, finally, to a velocity spectrum. A model of the velocity spectrum is fit to the observed spectrum to estimate the foam drift velocity. Confidence intervals and other measures of the input and output data quality are calculated. Field test comparisons were made against an in situ bidirectional electromagnetic current meter on the basis of 1 month of video data from the 1997 Sandy Duck field experiment. The root mean square error between the two approaches was 0.10 m/s. Linear regression analysis showed the gain between the two instruments to not be statistically different from one. Differences between the surface and interior measurements were compared to forcing mechanisms that may cause surface velocity shear. Velocity offsets and alongshore wind stress were well correlated for cases when waves and wind were not aligned to within ±45°, when wind- and wave-forced currents are reasonably separable. Calculated wind-dependent surface current shear, modeled as a surface boundary layer, correlated well with the observed velocity offsets for observations of nonalignment between wind and waves. This technique can be applied to study large-scale coastal behavior. *INDEX TERMS:* 4546 Oceanography: Physical: Nearshore processes; 4594 Oceanography: Physical: Instruments and techniques; *KEYWORDS:* longshore current, remote sensing, video

Citation: Chickadel, C. C., R. A. Holman, and M. H. Freilich, An optical technique for the measurement of longshore currents, *J. Geophys. Res.*, *108*(C11), 3364, doi:10.1029/2003JC001774, 2003.

1. Introduction

[2] The longshore transport of sediment is the single most important agent of coastal change along most of the world coastlines. Littoral drift can reach hundreds of thousands of cubic meters of sand per year [*Komar*, 1998]. Convergences and divergences of transport, caused by jetties, headlands or inlets, can yield large accretion or erosion rates, requiring expensive engineering mitigation. Even on a local scale, divergences of sediment transport over complex sandbars can yield local shoreline erosion and evolving bathymetric anomalies.

[3] Longshore transport is driven primarily by longshore mean currents. Thus an understanding of transport first requires a good understanding of the dynamics of longshore mean flows in the nearshore. This latter problem has received extensive study and was considered, in the mid-1980s, to be well understood. For longshore uniform conditions, currents are forced by radiation stress gradients associated with the dissipation of an obliquely approaching wave field [e.g., *Bowen*, 1969a; *Guza et al.*, 1986; *Longuet-Higgins*, 1970a, 1970b], while longshore variations in topography or incident wave conditions yield longshore pressure gradients, which, in turn, force longshore currents [e.g., *Bowen*, 1969b; *Munk and Traylor*, 1947; *Reniers*, 1999]. Direct wind forcing was found to have a secondary influence in the surf zone [*Feddersen et al.*, 1998]. However, recent work has illuminated further complications, particularly for the complex bathymetries that typify most natural beaches. *Bowen and Holman* [1989] and *Oltman-Shay et al.* [1989] discovered that longshore currents over barred bathymetries were unstable, producing large, very low-frequency oscillations called shear waves that, in turn, caused significant horizontal eddy mixing. Field observations of longshore currents on barred beaches often showed maxima in the bar trough, well away from the incident wave forcing maximum [*Reniers*, 1999]. In addition, work by *Lippmann and Holman* [1990] showed that sandbar systems are not commonly longshore uniform but instead typically feature evolving longshore structure and complexity. A consequence of these nonideal natural conditions is that accurate predictions of mean longshore currents and transport based on simple physical models may not be possible. Instead a combination of observation and modeling may be required. Indeed, as the complications of nearshore circulation over realistic bathymetries receive increasing focus, there will be an increasing need for extensive nearshore measurement campaigns.

[4] The traditional and most accurate method for longshore current measurement has been to use in situ instruments such as electromagnetic current meters or, more

0148-0227/03/2003JC001774$09.00

recently, acoustic sensors. These instruments are robust and well understood and provide accurate measurements. However, the high cost and the logistic difficulties of installing and maintaining arrays of such instruments has meant that they are better suited to intensive field campaigns rather than long-duration monitoring efforts. Similarly, array design usually requires compromises related to available budget and the inability to move instruments to adapt to changing bathymetry.

[5] Recently particle image velocimetry (PIV) techniques have been examined for measuring nearshore currents [*Holland et al.*, 2001]. Originally designed to estimate velocity by tracking small tracers in laboratory tanks, the correlation techniques work equally well in tracking advecting surface foam patterns in the surf zone. The PIV technique allows excellent spatial coverage of the surface flow field (in areas where foam is present) and is relatively low cost. However, traditional PIV methods require large computational effort and appear sensitive to tracking the bore front of breaking waves. They also require recording full video frames at moderately high temporal resolution O(1/10 s). This could impose data transmission problems for remote stations such as will be discussed below.

[6] The primary objective of this paper is to describe an alternative optically based method to measure surface longshore currents. As with PIV, this optical current meter (OCM) exploits the naturally present drifting sea foam left after the passage of breaking waves, and thus enjoys the advantages of low-cost, logistic ease, wide coverage and sampling flexibility. This new OCM method is based on the time-space characteristics of foam traces from an alongshore oriented transect of image pixels, and thus allows low data rate communications. Individual foam traces are not used; instead the bulk frequency-longshore wave number spectrum of a sample time-space window is analyzed.

[7] In sections 2 and 3, the technique is described and tested using synthetic data. In section 4, OCM measurements are compared to in situ data collected during the SandyDuck field experiment in 1997, followed by discussion in section 5.

2. Optical Current Meter Technique

[8] The optical current meter is just one of a suite of techniques that exploit the range of visible signatures available in the nearshore. Similar visible imagery has been used to measure: the period and direction of breaking waves [*Lippmann and Holman*, 1991], run-up time series [e.g., *Holland and Holman*, 1993], nearshore bathymetry [*Stockdon and Holman*, 2000], the time-varying location of the shoreline [*Plant and Holman*, 1997] and the location and morphology of submerged sandbars [*Lippmann and Holman*, 1989]. Video data collection has been based on unmanned, shore-based monitoring platforms called Argus Stations [*Holman et al.*, 1993].

[9] Key to all video methods is knowledge of the transformation from image (U, V) to real world (x, y, z) coordinates (our coordinate system used throughout this paper is right-handed with the x axis perpendicular to the shoreline and increasing offshore). The geometry of a particular camera installation is found through the use of a set of visible ground control points with known locations [*Holland et al.*, 1997]. Resulting transformations are typically found to be accurate to the nearest pixel. For the conditions described below, the mean pixel resolution in the alongshore and cross-shore directions are 0.25 and 0.45 m, respectively.

Snapshot

Figure 1. Snapshot of the surf zone at Duck, North Carolina, on 2 October 1997. The line indicates the location of an alongshore pixel array where video record (Figure 2) was taken.

[10] For the determination of alongshore surface velocities, video data are collected from an alongshore oriented array of pixels (Figure 1). Observations of foam patch sizes show the dominant wavelengths of natural foam to lie between 1 and 10 m (e.g., Figure 1). Thus an alongshore pixel spacing and overall array length were chosen to be 0.25 and 30 m, respectively, which allows for adequate resolution of the expected foam wavelengths in the frequency domain.

[11] The video data, $I(y, t; x)$, consists of time series of pixel intensity on a 256 level gray scale from each pixel in the alongshore array at some cross-shore location, x, and is digitized on site by an SGI O2 Unix workstation. The data are recorded at 2 Hz sampling (15 video frame increments) for 1024 s duration. An example image of $I(y, t; x)$, called a timestack, is seen in Figure 2.

2.1. OCM Algorithm

[12] The OCM produces a robust and accurate estimate of the magnitude and direction of the mean surface longshore current for the length of window of analysis, along with an estimate of the error. In addition, objective criteria are developed and tested to identify data segments for which no useful estimation can be made.

[13] The algorithm consists of four steps: computation of a two dimensional frequency-wave number spectrum; transformation of the spectrum into a wave number-velocity spectrum; integration over wave number to produce a velocity spectrum (the distribution of image intensity variance with estimated velocity); and finally estimation of a single most representative velocity for that segment.

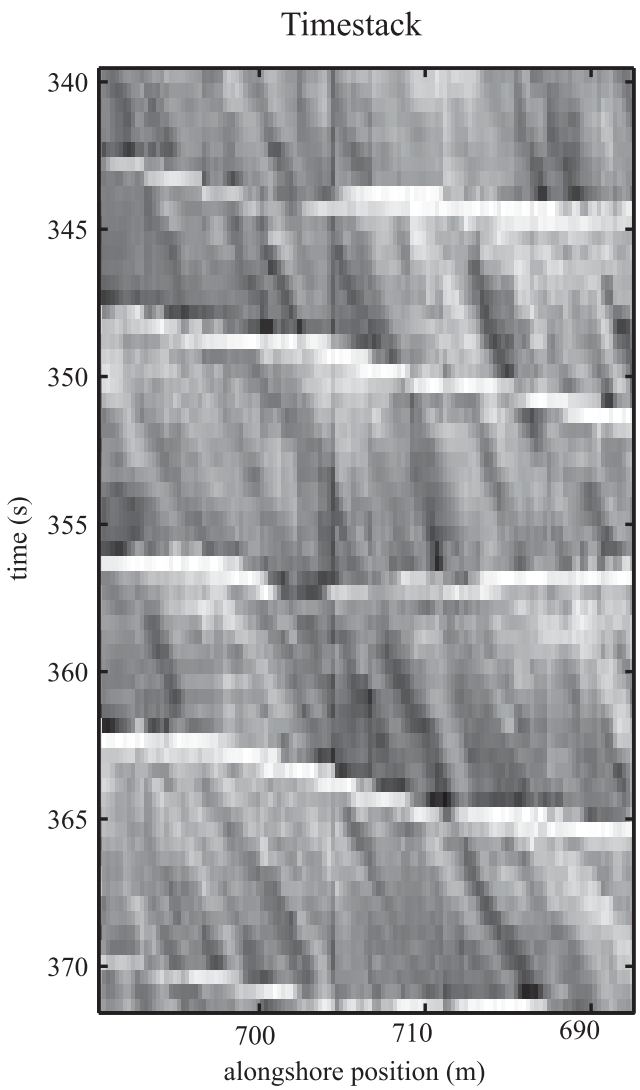

Figure 2. A time series of pixel intensities from the alongshore array of pixels in Figure 1. The record, called a timestack, reveals the bright horizontal bands of passing breaking waves and the oblique traces of foam patches drifting with the prevailing longshore current.

The discussion below will be based on the timestack in Figure 2.

2.2. $S(f, k_y)$ Calculation

[14] The initial step is to transform the video pixel intensity data, $I(t, y;x)$, from the space (y) and time (t) domain to a frequency-alongshore wave number $\hat{I}(f, k_y; x)$ domain using a two dimensional Fourier transform,

$$\hat{I}(f,k_y;x) = \int\int B(t,y)I(t,y;x)e^{-i2\pi ft}e^{-i2\pi k_y y}dtdy. \quad (1)$$

where f is frequency (Hz) and k_y is alongshore wave number (1/m). The input data are simultaneously windowed with a two dimensional Bartlett multiplicative filter, $B(t, y)$, [*Press et al.*, 1992] to reduce leakage in the spectrum. The two-dimensional spectrum, $S(f, k_y)$, is computed as

$$S(f,k_y) = \hat{I}(f,k_y)\hat{I}(f,k_y)* \quad (2)$$

where the asterisk (*) denotes the complex conjugate.

[15] Figure 3 shows $S(f, k_y)$ calculated from the sample timestack from Figure 2. Features in the original timestack image have analogs in the spectrum. The horizontally oriented bright bands in the time series are caused by passing breaking waves and appear in the f-k_y spectrum as energy distributed near zero wave number (the abscissa in Figure 3). Since (y directed) longshore velocity is the ratio of frequency to wave number, lines of constant velocity are represented as rays extending from the origin of the spectrum, with slope inversely proportional to velocity. Negative velocities are associated with negative frequencies, and positive velocities with positive frequencies. Because residual foam in the surf zone has a broad distribution of characteristic wavelengths, the energy representing the oblique traces of foam streaks advecting at constant velocity lie generally along a ray from the origin, extending through many wave numbers and frequencies.

2.3. $S(v, k_y)$ Transformation

[16] The spectrum is then transformed from frequency-wave number space to velocity-wave number space using the mapping $v = f/k_y$. To conserve variance, the transformation is

$$\mathrm{var}\{S(f,k_y)\} = \int\int S(f,k_y)dfdk_y = \int\int S(v,k_y)|k|\,dv\,dk_y \quad (3)$$

where $|k|$ is the Jacobian determinant and $S(v, k_y)$ is the velocity-wave number spectrum (Figure 4). To eliminate possible contamination resulting from obliquely incident waves which mimic rapidly moving sea foam, the

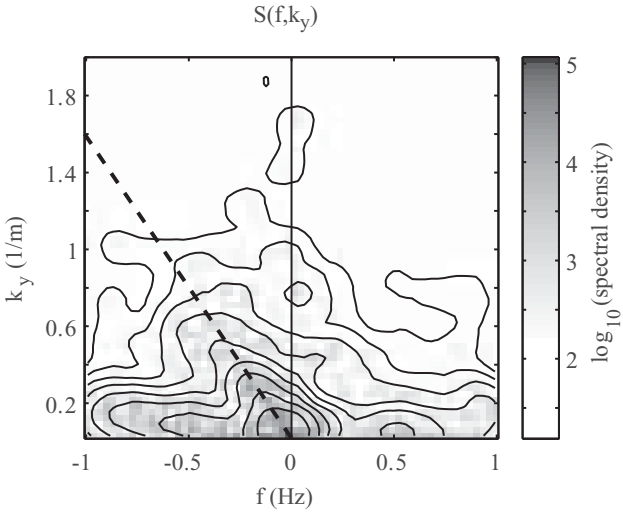

Figure 3. Frequency-wave number spectrum of the timestack in Figure 2. Note the concentration of energy along the dashed line corresponding to a constant velocity of −0.6 m/s.

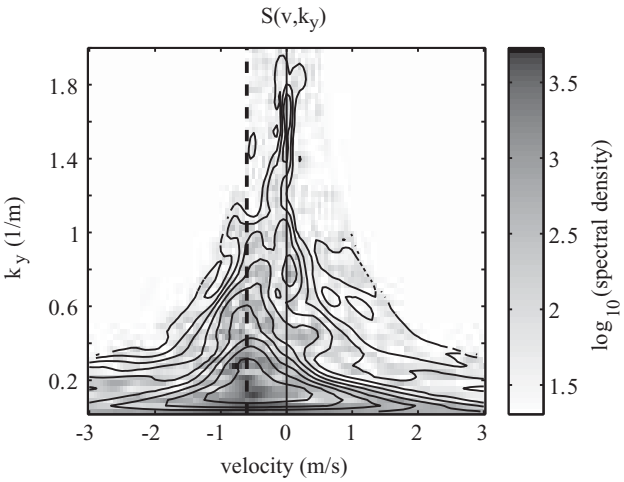

Figure 4. $S(v, k_y)$ spectrum shows a concentration of energy at about 0.6 m/s in wave number-velocity space.

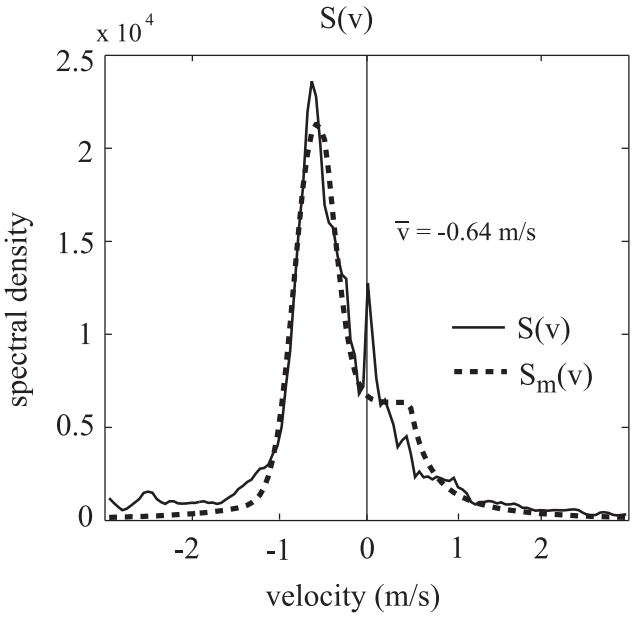

Figure 5. $S(v)$ spectrum derived from Figure 4. The modeled velocity and the final fit returned from the nonlinear fitting routine are also plotted.

integration is carried out only over frequency and wave number ranges such that the velocity is constrained to lie between ±3 m/s. The alongshore projection of wave speed for an oblique wave is usually well out of this range while longshore currents are typically within this range. In Figure 4, the resulting spectrum indicates a concentration of energy corresponding to an apparent current of about 0.6 m/s. The regions of no data in the velocity extremes at higher wave numbers are due to the extension of our mapping bounds beyond the original $S(f, k_y)$ spectrum (beyond the Nyquist frequency) and are set to zero.

2.4. $S(v)$ Transformation

[17] The $S(v, k_y)$ spectrum can be integrated with respect to wave number over the region of valid data, yielding a velocity "spectrum"

$$S(v) = \int_{k_{\min}}^{k_{nyq}} S(v, k_y)\, dk_y. \tag{4}$$

Leakage of energy into $S(v)$ from oblique wave crests is manifested most obviously as increased spectral energy at large v and low wave number. This contamination is minimized by excluding energy at wave numbers below the wave number minimum, k_{min} (chosen here as 0.125 m^{-1}). The upper limit of the integral is the Nyquist wave number, k_{nyq}, or $1/(2dy)$, where dy is the alongshore sampling spacing. The resulting velocity spectrum (Figure 5) has several typical features: a background energy level due to video noise and low-frequency intensity patterns and a relatively large peak of energy representing the foam traces.

2.5. $S(v)$ Model

[18] Because the $S(v)$ spectrum is composed of a complicated mix of energy from foam streaks, waves and background noise, it not trivial to determine a single surface velocity estimate. Methods to estimate a representative velocity on the basis of bulk statistics of the velocity spectrum (e.g., the mean or median velocity) are biased by residual background energy leaked from waves and by the transformed impact of a white noise background in f-k_y space, discussed below. Just as problematic is utilizing the location of the maximum energy or largest peak as a velocity estimate, because spurious large, but narrow peaks are not uncommon in the $S(v)$ spectrum.

[19] The OCM method instead uses a nonlinear least squares routine to fit a model of the velocity spectrum, $S_m(v)$, to the observed spectrum, $S(v)$. Since wave energy has largely been eliminated, our model includes two com-

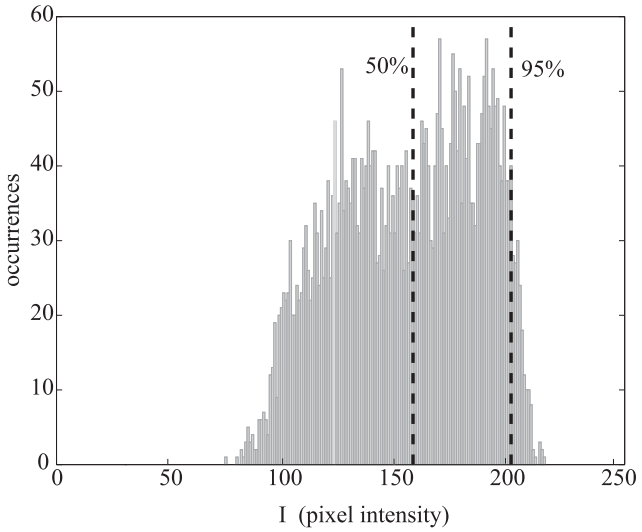

Figure 6. The sample histogram from a 32-s section of a timestack shows a broad range of image intensity. The dashed lines represent the 50th and 95th percentile intensities.

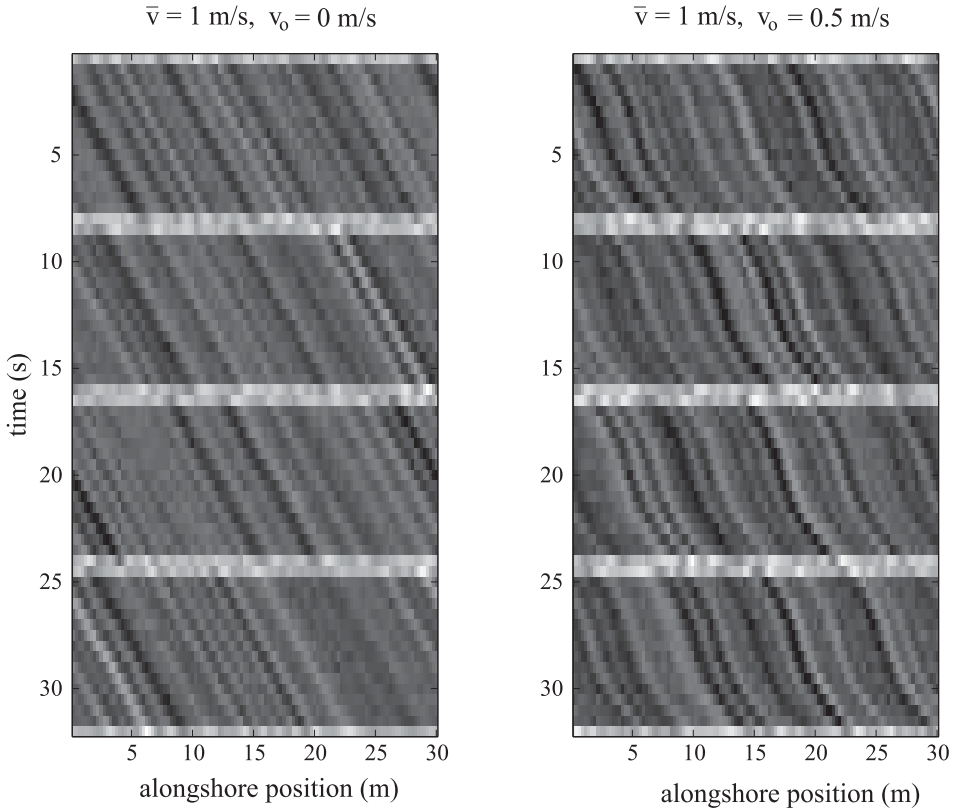

Figure 7. Synthetic stack examples: (left) an example of a synthetic timestack with advected foam (oblique traces) moving at a constant 1 m/s and breaking waves (horizontal bright lines) and (right) foam advecting at an average of 1 m/s with an added sinusoidal velocity variation with amplitude 0.5 m/s.

ponents, the signature of the background noise and that for oblique foam traces

$$S_m(v) = S_{foam}(v) + S_{noise}(v). \tag{5}$$

The foam trace spectrum, S_{foam}, is modeled as a Gaussian with amplitude A_{foam}, mean foam velocity $\bar{v}$ and width σ_{foam}

$$S_{foam}(v) = A_{foam} \exp\left[-\frac{(v-\bar{v})^2}{\sigma_{foam}^2}\right]. \tag{6}$$

A noise background is derived by assuming an input white noise pixel intensity time series, with energy distributed uniformly over $S(f, k_y)$. Transforming this white noise to the velocity spectrum yields

$$S_{noise}(v) = \begin{cases} A_{noise}\dfrac{f_{nyq}^2}{2v^2} & \text{for } |v| \le \dfrac{f_{nyq}}{k_{nyq}} \\ A_{noise}\dfrac{k_{nyq}^2}{2} & \text{for } |v| > \dfrac{f_{nyq}}{k_{nyq}} \end{cases}. \tag{7}$$

In the $S_{noise}(v)$ model A_{noise} is the noise amplitude factor, f_{nyq} and k_{nyq} are the sampling-dependent Nyquist frequency and Nyquist wave number, respectively.

[20] The model thus depends on four parameters, A_{foam}, $\bar{v}$, σ_{foam}, and A_{noise}. An initial guess of the fitting parameters from (6) and (7) is generated using basic statistics of $S(v)$ and is passed, along with $S(v)$, to the nonlinear fitting routine. Parameters are initialized as follows. A_{foam} is taken as the peak energy value in $S(v)$, $\bar{v}$ as the velocity value corresponding to the energy peak, σ_{foam} is guessed as 0.15 m/s and A_{noise} is initially chosen to be the median value of $S(v)$. The fitting routine uses the Gauss-Newton method

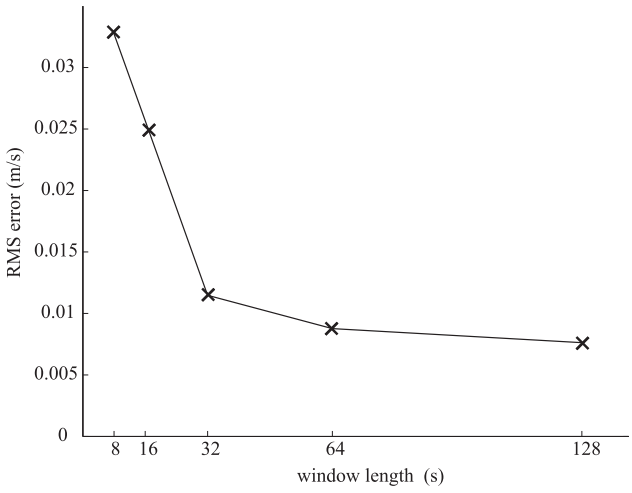

Figure 8. Total root mean square error for each window length, T_l, over all mean velocities and maximum orbital velocities.

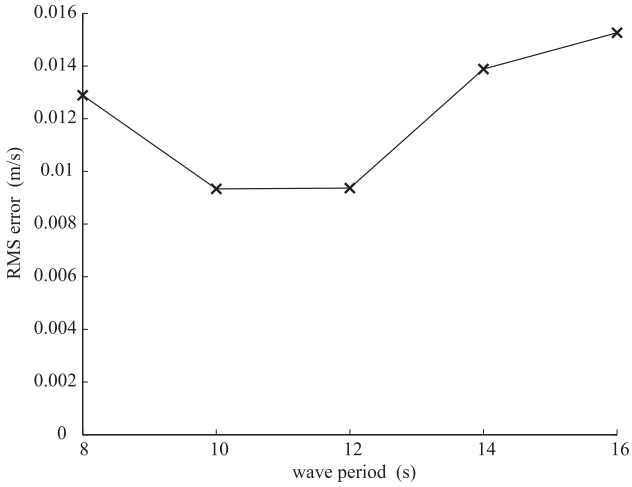

Figure 9. Total root mean square error for each wave period for all mean velocities and orbital velocity amplitudes, based on a sample window length of 32 s.

to iterate to a best fit solution in the least squares sense [*Press et al.*, 1992].

2.6. Calculating a Longshore Current Velocity Time Series

[21] A time series of longshore current velocity, v, can be estimated by applying the OCM algorithm repeatedly in a stepwise fashion through a long video record, so that the window of analysis overlaps the previous window by some amount of time. The time length of the analysis window, T_l, and the time length of the step, T_s, are both unrestricted constants. Increasing T_l increases the stability of the resulting estimate, but decreases the temporal resolution of the alongshore velocity time series.

2.7. Velocity Estimate Quality

[22] The quality of the velocity estimate derived from the OCM algorithm was assessed by computing statistical measures of the "goodness of fit" of the model and the best fit parameters to the data. Additionally, because this method is based on the presence of foam due to wave breaking, a method was devised to provide an objective filter to identify and reject estimates calculated from images which did not contain sufficient foam contrast. These quality measures provide a basis for disregarding cases for which no useful result is expected.

[23] The quality of the model fit to the data is described using a χ^2 statistic [*Press et al.*, 1992]

$$\chi^2 = \sum_{i=1}^{N} \left[\frac{S(v(i)) - S_m\left(v(i); \hat{\beta}\right)}{\sigma(i)} \right]^2 \tag{8}$$

where $\hat{\beta}$ are the set of the "best fit" parameters and $\sigma(i)$ is the standard deviation of the measurement error at each point i. In the case of the OCM the measurement error is unknown a priori. We choose to assign $\sigma(i)$ as a constant for all i, 10% of the maximum value of $S(v)$, which allows for an objective measure of the statistical significance of the model fit regardless of total energy, which is expected to vary depending on the lighting condition and camera settings.

[24] Ninety-five percent confidence intervals on the model parameters, β, are estimated independently on the basis of a quadratic fit of the surface due to the sum of squares of the residuals in the vicinity of the "best fit" parameters, determined from the nonlinear least squares fit [*Press et al.*, 1992].

[25] We calculate a proxy for the degree of breaking and residual foam in the video record, I_{range}, based on the intensity histogram of a window of the timestack

$$I_{range} = I_{95} - I_{50} \tag{9}$$

where I_{95} and I_{50}, are the 95th and 50th percentile intensity values, respectively. Figure 6 shows the intensity histogram of the section of timestack from Figure 2. As the value of I_{range} increases, so does the contrast and the degree of wave breaking and residual foam seen in the timestack. A threshold value for usable data is investigated in section 4.

2.8. Viewing Angle Velocity Bias

[26] The OCM approach assumes the pixel array to be at mean sea level over the duration of the analysis window. If this were true, the longshore current velocity estimate would be unbiased, but time-dependent departures from mean sea level due to the presence of waves will cause a change in the apparent horizontal position of any pixel. Thus a rate of change of sea surface elevation will appear as an apparent longshore surface velocity. This apparent velocity will bias the estimated longshore current velocity in an additive way that would average to zero if foam variance were distributed uniformly over the wave however, we only receive useful foam traces from the back of the wave. The bright intensity band of a passing turbulent wave front (Figure 2), associated with the front face of the wave, contributes a spectral signature that is outside of the f-k_y domain of advected foam and is excluded (discussed above), thus a mean bias can be introduced. In this section we present a simple model of the velocity bias in order to correct optical current meter estimates.

[27] The model follows the standard pinhole camera assumption that light rays travel in straight lines from the observed real world objects, through a focal point, to the image plane [*Wolf and Dewitt*, 2000]. The camera's pinhole is located at (x_c, y_c, z_c) and the point being observed in the real world is at (x_p, y_p, z_p). The parametric equations for the line of sight from the camera to the point of observation in space are:

$$x = x_c + s\left(x_p - x_c\right) \tag{10a}$$

$$y = y_c + s\left(y_p - y_c\right) \tag{10b}$$

Table 1. Wave and Wind Conditions During SandyDuck

	Mean	Maximum	Minimum
H_0, m	0.98	3.44	0.31
T_p, s	9.3	15.6	3.7
α,[a] deg	3.7	51.6	−34.6
W, m/s	5.5	18.4	0.03

[a]Positive angles indicated waves arriving from the north.

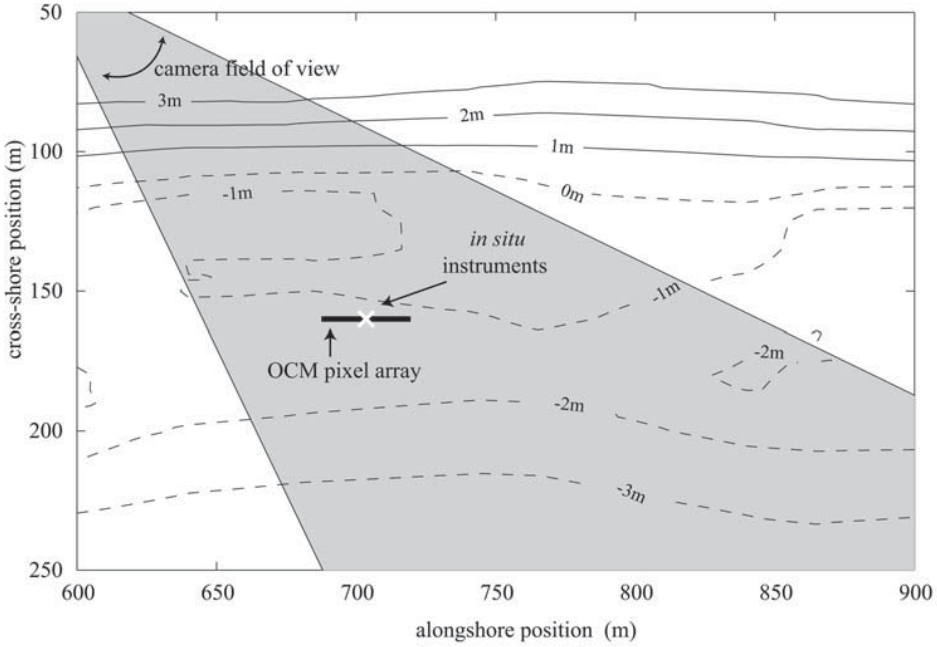

Figure 10. Plan view of the collocated current meters and pressure sensors, bathymetry, and OCM pixel array.

$$z = z_c + s(z_p - z_c), \tag{10c}$$

expressed in terms of the dummy variable s.

[28] For simplicity, the variable sea surface is modeled as a regular saw tooth wave, incident at angle α, such that there is a discontinuous finite jump where the trough of the previous wave immediately precedes the next crest. The shape of the free water surface for one wave period is:

$$z = \frac{-H[(x - Ct)\cos(\alpha) - (y - Ct)\sin(\alpha)]}{L} + \left(z_0 - \frac{H}{2}\right) \quad \text{for } 0 \le t < T \tag{11}$$

where C is the wave celerity and T is the wave period, H is wave height, L is wavelength, and z_0 is the mean sea level.

[29] The rate of change of the alongshore position, $v_{apparent}$, of the intersection of the camera's line of sight with the moving wave surface with respect to time is calculated from (10) and (11) by solving for y and differentiating in time:

$$v_{apparent} = \frac{CH(y_p - y_c)}{H\left[(x_p - x_c)\cos(\alpha) + (y_p - y_c)\sin(\alpha)\right] + L(z_p - z_c)}. \tag{12}$$

The solution describes the apparent rate of change of longshore viewing position due to the passing wave. Thus a patch of foam at a fixed longshore location would appear to move in the opposite sense, and a correction can be applied to the mean velocity estimates as

$$v_s = \overline{v}_{OCM} - v_{apparent}. \tag{13}$$

Discussion of the magnitudes and the nature of this correction for the test cases occurs in § 4.

3. Synthetic Data Tests

[30] This section tests the performance of the OCM algorithm for different analysis window lengths, T_l, by applying the OCM to synthetic data sets for which the breaking, foam patterns and longshore current properties are known precisely.

[31] Idealized timestacks were constructed to include the alongshore drift of sea foam driven by the superposition of a mean longshore current and the alongshore component of surface wave orbital velocity, as well as the visual signature of the shoreward propagating breaking wave front. The time variation of the longshore velocity field was modeled as

$$v(t) = \overline{v} + v_o \cos\left(\frac{2\pi t}{T}\right), \tag{14}$$

where v_o is the alongshore wave orbital amplitude and T is wave period. Surface foam was assumed to drift with the same velocity as the longshore current with no time lag.

[32] Foam streaks were modeled as the sum of sinusoidal variations in the image intensity in the alongshore direction. Since a range of characteristic sea foam wavelengths exists in a natural surf zone environment, a uniform distribution of energy over wavelengths from 2 to 15 meters was assumed. The pattern of foam patches was regenerated with new random phases after the passage of each breaking wave crest. The passing wave front was depicted as a monochromatic wave field, with a bright horizontal band of constant intensity appearing in the timestack at every integer multiple of the wave period. Finally random image intensity noise

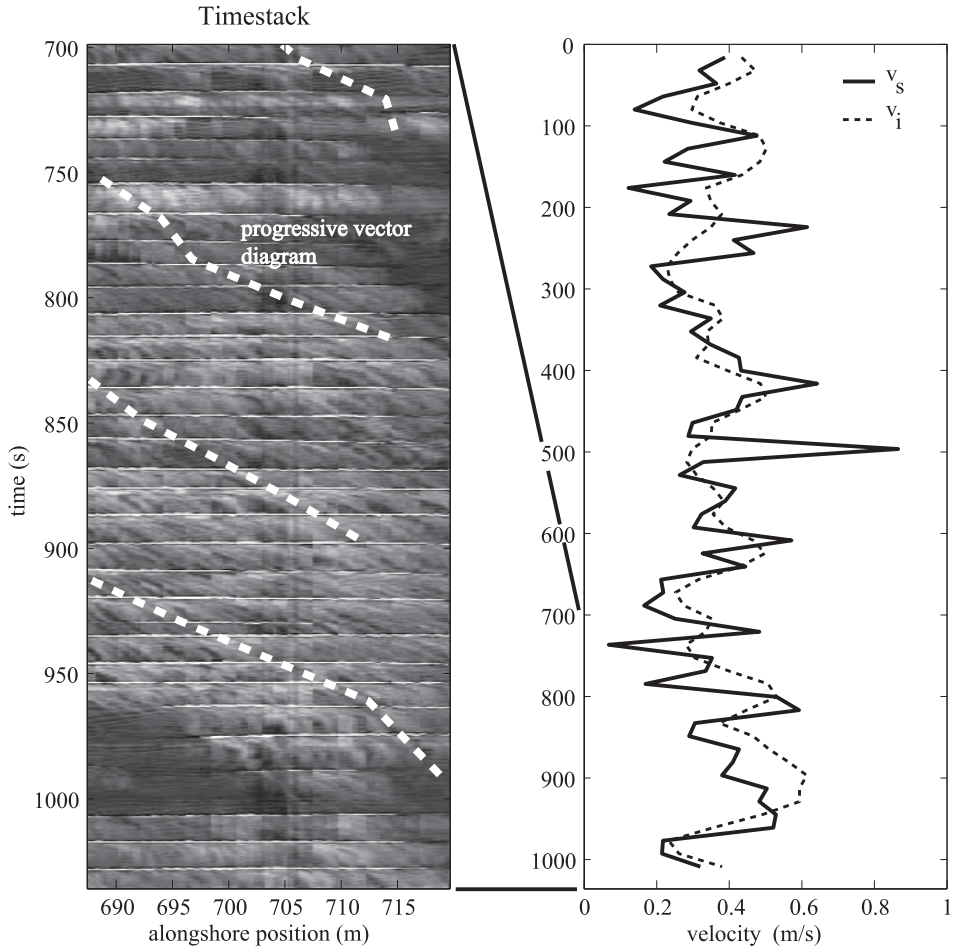

Figure 11. (left) Sample timestack with superimposed progressive vector diagram (PVD) and (right) longshore current time series. The PVD is the stepwise-integrated surface velocity time series and shows good alignment with foam streaks. Note that the timestack and PVD are only a portion of the full 1024-s timestack. The data were taken on 4 November at 2034 GMT.

was added to the stack. Two examples of synthetic stacks are shown in Figure 7.

[33] Synthetic stacks with a constant wave period of 8 s were created using a range of mean longshore velocities from 0 to 1.5 m/s, the typical range observed in the field. The alongshore orbital velocity amplitude was allowed to vary from 0 to 0.5 m/s, to simulate varying degrees of contamination by obliquely incident waves. The maximum value of 0.5 m/s corresponds to a shallow water wave with a height of 1 m approaching the shoreline at 27° from normal or a 2-m wave approaching at 13° from normal incidence.

[34] The OCM algorithm was applied to each synthetic stack using different analysis window lengths, T_l. The choices for T_l initially included an integral number of wave periods from 8 to 64 s in increments of 8 s. Subsequent tests explored OCM performance for nonintegral wave period sampling. Ten realizations of the synthetic timestacks were created for each combination of T_l, $\bar{v}$ and v_o. The root mean square (rms) error between the optically estimated and true mean velocity was then computed. Figure 8 shows that the total RMS error was low (under 0.035 m/s) for all choices of T_l. It is also apparent that as T_l is increased, the accuracy of the OCM increased for all mean velocities considered, although there was little change for T_l larger than 32 s.

[35] A second test was conducted with synthetic timestacks with monochromatic waves of varying wave period (8, 10, 12, 14, and 16 s), and T_l = 32 s to determine if noninteger wave period sampling has an effect on the velocity estimation. Ten timestacks for each combination of T, $\bar{v}$ and v_o were created, the mean current was estimated, the results were averaged and the RMS error was calculated for each choice of T. The RMS error (Figure 9) for this test is less than 0.02 m/s over the range of simulated conditions. Presumably, longer runs will yield reduced bias for sample lengths that are not integer multiples of the wave period. The final choice of T_l balances the RMS error reduction gained by using longer T_l, with the increased temporal resolution gained by using shorter T_l. For this reason, subsequent analyses are based on T_l equal to 32 s, as little error reduction was gained by doubling the window length to 64 s.

4. Field Test

[36] The optical current meter technique was tested by comparing OCM estimates of the mean longshore current

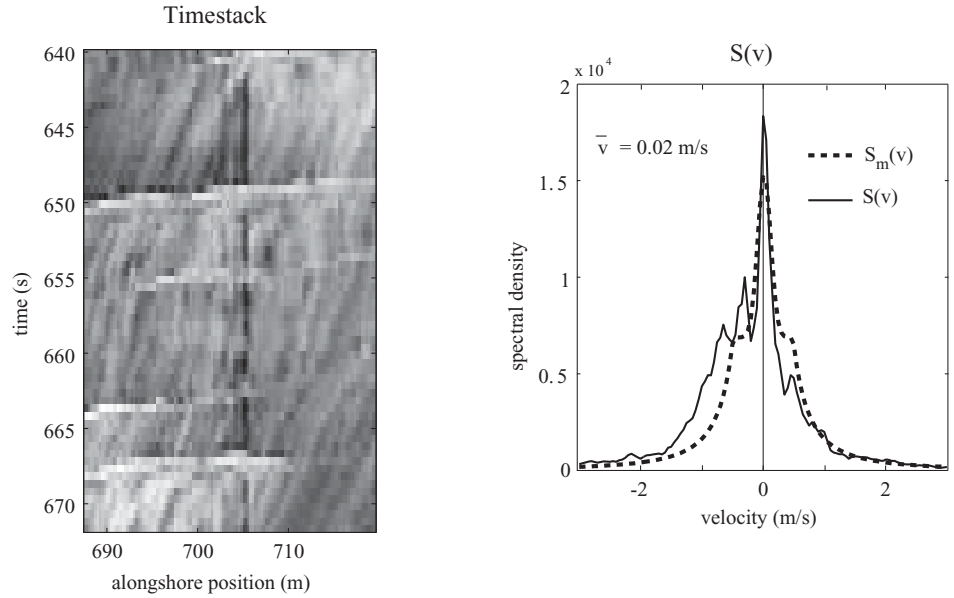

Figure 12. (left) A section of a timestack taken on 2 October at 1534 GMT. It shows the contamination of the in situ sensor frame as dark vertical traces. (right) The resulting velocity spectrum and velocity model fit are shown.

with mean longshore currents measured by an in situ current meter. While the optically based current meter measures the surface expression of the longshore current, conventional current meters (e.g., electromagnetic, acoustic and impeller types) necessarily sample the interior currents, so comparisons between the two are not direct. However, previous studies [e.g., *Garcez Faria et al.*, 1998] have shown that there is little vertical shear in longshore currents except near the seafloor.

[37] The field test was conducted at the Field Research Facility (FRF) in Duck, North Carolina [*Birkemeier et al.*, 1985], during the 1997 SandyDuck Field Experiment [*Birkemeier et al.*, 1996]. Data for the comparison spanned the time from 1 October 1997 to 11 November 1997. Wave directional and frequency spectra were derived from 3-hour records of surface elevation time series recorded from a 15 element array of pressure sensors located in 8-m depth, approximately 900 m offshore of the FRF [*Long and Oltman-Shay*, 1991]. From these direction-frequency spectra a measure of the resultant wave direction α is estimated. Mean wind speed and direction measurements were collected from a meteorological station at the end of

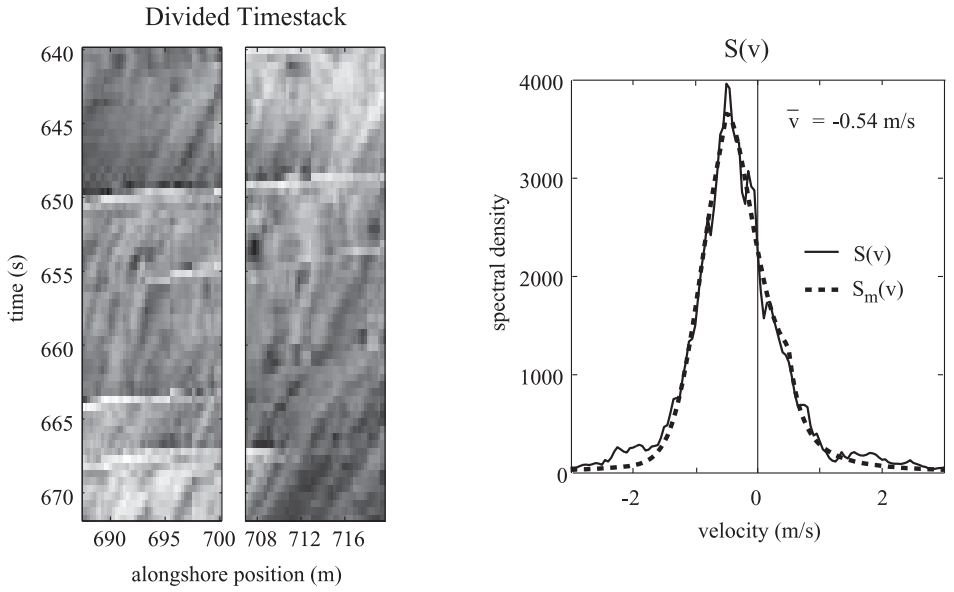

Figure 13. (left) The same stack from Figure 12, with the contaminated middle section removed. (right) The resulting $S(v)$ derived from the average of the $S(f, k_y)$ spectrum from each separate subtimestack.

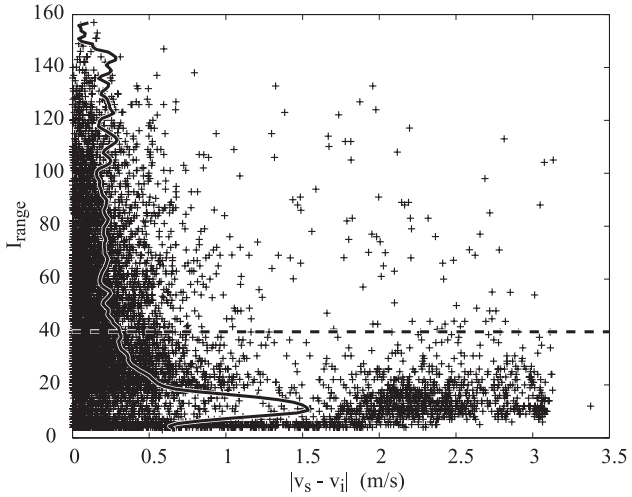

Figure 14. I_{range} variable compared with the absolute deviation of surface currents from interior longshore currents. I_{range} is the intensity span from the 95% to the median intensity value. The curve is the interpolated value of velocity discrepancies over the span of I_{range}. A dashed line indicates the threshold value of I_{range} = 40 used to determine the presence of adequate contrast (i.e., foam streaks) in the timestack.

the FRF pier at a height of 19.36 m. These measurements were converted to estimates of alongshore wind stress, using [*Taylor*, 1916]

$$T_y^{wind} = C_d \rho_a |w| w_y \tag{15}$$

where ρ_a is the density of air, w the wind velocity, w_y the longshore component of that velocity (both corrected to 10-m elevation) and C_d the drag coefficient as formulated by *Large and Pond* [1981]. Negative wind stress is a result of winds from the positive y (alongshore) direction. Offshore wave (peak wave period, T, significant wave height H_0, and wave angle, α) and wind speed conditions during the field experiment are summarized in Table 1.

[38] As part of SandyDuck, a team led by Steve Elgar and Robert Guza collected measurements in the surf zone using an array of bidirectional electromagnetic current meters and pressure sensors [*Elgar et al.*, 2001]. Data for the comparison here comes from one of their 33 locations (location '11'; Figure 10). Electromagnetic current meter measurements of longshore velocity, cross-shore velocity and surface elevation were recorded at 2 Hz in 3-hour continuous blocks with slight gaps between blocks. The vertical position of the current meter was adjusted to maintain a nominal position in the midwater column, with a minimum distance from the seabed of 57 cm and a mean position of 95 cm from the bed, while the total mean water level during the experiment was 1.8 m. To guard against contamination due to the periodic emergence of the instruments at low tide, data runs for which the significant wave amplitude (half the significant wave height) was greater than the mean water depth above the current meter, both quantities calculated from the collocated pressure sensor measurements, were removed from consideration.

[39] The time series of in situ longshore current measurements (v_s) was smoothed with a running boxcar window with a window length equal to T_l (the analysis window length in the OCM algorithm) and subsampled with sampling spacing of T_s to match the sample spacing and

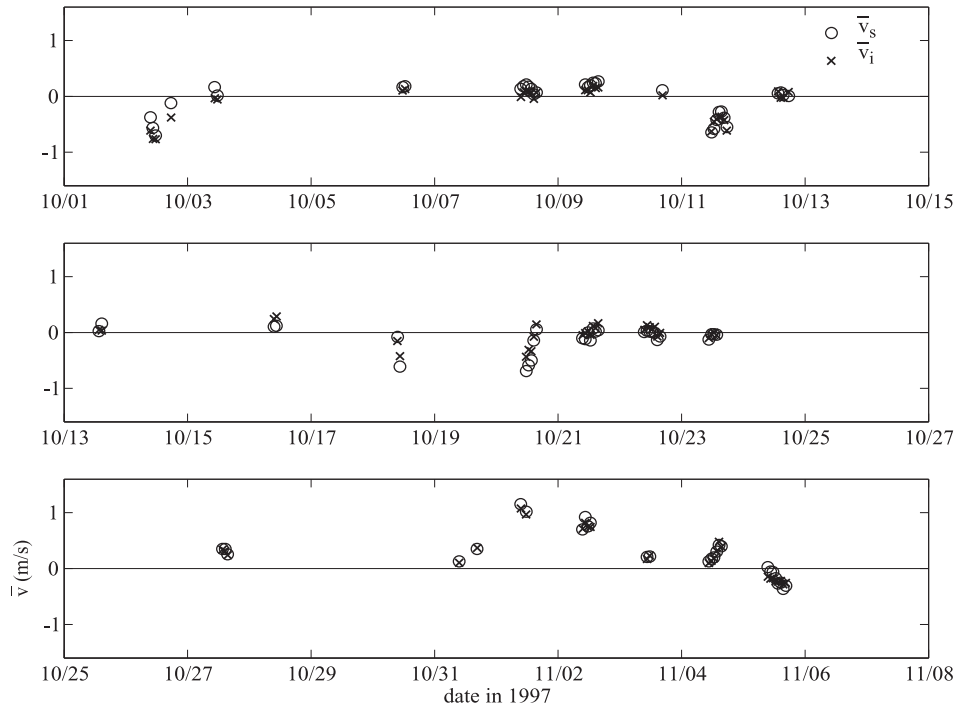

Figure 15. Optically measured mean surface currents (circles) and in situ currents (crosses) for October and the first week of November 1997 at Duck, North Carolina.

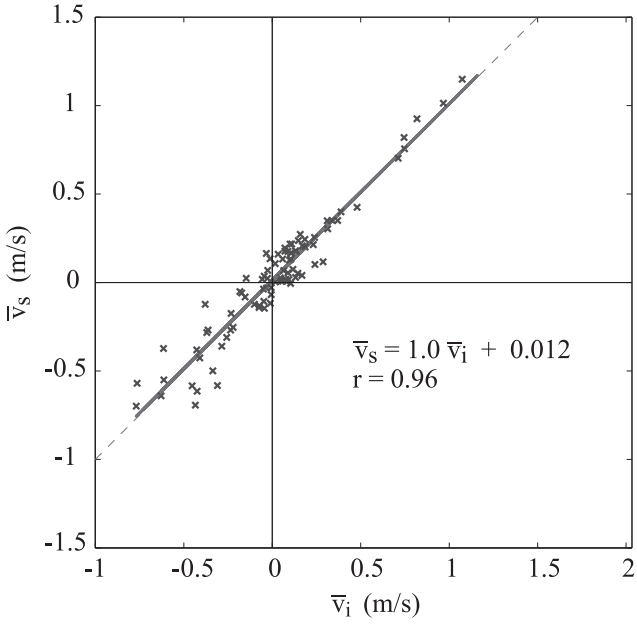

Figure 16. In situ longshore current means, $\overline{v}_i$, versus surface longshore current means, $\overline{v}_s$. A linear least squares regression is shown as the thick line, and a perfect fit 1:1 line is shown as the dashed line.

smoothing characteristics of the OCM time series. Subsections of the smoothed and subsampled v_i time series corresponding to the individual 17-min OCM records were then extracted for the ground truth comparison.

[40] Information used to calculate the other wave based parameters were taken from the in situ pressure sensor records. The standard deviation of the water surface elevation time series, σ_η, was calculated and used to estimate the mean wave height [*Dean and Dalrymple*, 1984], using

$$\overline{H} = 2.5035\ \sigma_\eta. \tag{16}$$

The wave celerity was calculated using shallow water linear wave theory wave

$$C = \sqrt{gh} \tag{17}$$

where h is the local water depth. The wavelength, L, is calculated using

$$L = CT_p \tag{18}$$

where T_p is the peak wave period estimated from the frequency spectrum of the in situ pressure sensor records [*Jenkins and Watts*, 1968].

[41] Simultaneous video data were collected from an OCM pixel array centered on the horizontal location of the in situ instrument cluster '11' (Figure 10 and pictured in Figure 1). The vertical coordinate of the pixel array was determined from the predicted tide level at the time the video data were recorded. Video timestacks were collected during daylight hours, once each hour for 1024 s (17 min) at 2 Hz from 1 October to 11 November 1997.

[42] Prior to processing, timestacks with poor video quality were identified and eliminated. The most prevalent problems of sun glare and low ambient light levels at dusk were treated by removing video data runs between the hours of 1700 and 0900 EST. A less common problem, rain on the camera lens, could not be detected automatically and required a manual search. Data obtained on three days (15, 19, and 26 October) were removed because of rain contamination.

[43] A time series of surface longshore current, v_s, was estimated using the OCM algorithm for each (hourly) 17-min record. The analysis window length, T_l, was set to 32 s and the time step, T_s, was 16 s (for a 50% overlap). This produced a 63 point time series of surface longshore current for each individual 17-min video record (e.g., Figure 11).

[44] The alongshore pixel array was centered on the horizontal real world location of the in situ current meter, which is mounted on a dark metal frame. Unfortunately, at low tide the frame was exposed and was sampled as part of the video data. This resulted in a long dark trace at a fixed longshore coordinate throughout the timestack (e.g., Figure 12). When a stack contaminated in this way was analyzed with the OCM algorithm, the vertical feature caused by the dark unmoving frame produced a velocity estimate that was biased low, and often produced a zero velocity estimate even when foam streak traces dictated otherwise (Figure 12).

[45] This problem was circumvented by splitting every timestack into two equal sections in the alongshore (spatial) direction, one on either side of the contaminated middle section, omitting the central section from y = 701 to 707 m. $S(f, k_y)$ spectra were computed from each subtimestack independently and averaged. An example of a divided stack and the resulting $S(v)$ spectrum is shown in Figure 13.

[46] In the absence of a theoretical threshold value for I_{range} (equation (9)) the threshold was chosen empirically. Figure 14 shows the distribution of absolute differences of the optically calculated surface longshore velocities and the in situ longshore velocities, as a function of I_{range}. It is clear that v_{diff} decreased with increasing I_{range}, indicating the

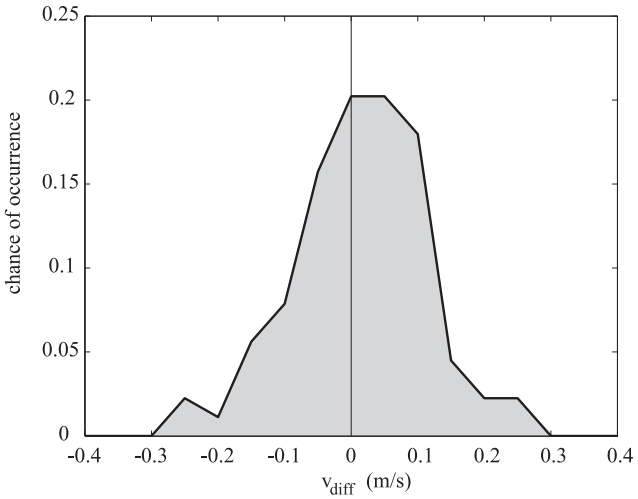

Figure 17. Probability density plot of the difference between mean surface and interior longshore currents, v_{diff}.

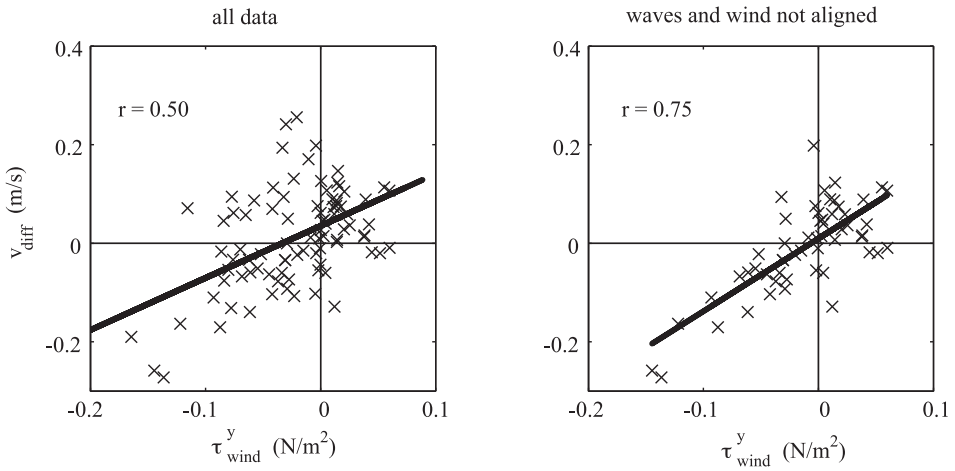

Figure 18. The v_{diff} compared to the alongshore component of wind stress: (left) all of the data and (right) data for observations where wind and waves are not aligned to within ±45°. Linear least squares regressions are plotted as solid lines in each panel along with the skill values.

increased accuracy of the OCM with increasing contrast, which we attribute to the increased presence of residual foam. A calculation of the interpolated v_{diff} over the span of I_{range} yielded a curve with a distinguishable increase for values of I_{range} less than 40 (Figure 14). This value was selected as the threshold of I_{range} for acceptable data, was used for the remainder of the tests and is recommended for future analyses.

[47] Individual OCM estimates of the surface velocity, v_s, were deemed acceptable if they satisfied three criteria: (1) greater than a 90% significance of fit from the model skill (§ 2); (2) a 95% confidence range of less than 0.2 m/s (± 0.1 m/s, § 2); and (3) $I_{range} > 40$ (§ 4). Mean currents were considered valid if at least 10 of the 63 estimates for each time series passed the above criteria.

4.1. Results

[48] An acceptable mean velocity was calculated for 109 of the 307 valid stacks collected in the comparison experiment. Figure 15 shows a time series comparison of mean longshore current estimates from the optical current meter with ground truth data returned from the in situ longshore current meter. The mean OCM longshore surface currents, $\overline{v}_s$, and in situ longshore currents, $\overline{v}_i$, correspond closely in magnitude and sign for the majority of the record.

[49] A more direct comparison between the two estimates is shown in Figure 16, where $\overline{v}_s$ is plotted versus $\overline{v}_i$. Were the surface and interior velocity estimates in perfect agreement the data would lie along the line of unity slope. The overall agreement between the two is very good with little scatter and with a significant linear least squares fit having slope 1.0 ± 0.1 (95% confidence limit) and intercept 0.01 m/s. The fitted parameters are not statistically different from a linear regression with slope 1 and intercept 0, at the 95% significance level, as interpreted from an F test [*Bendat and Piersol*, 1986].

[50] A histogram of the differences between hourly 17-min mean velocities for both optical and in situ measurements is plotted in Figure 17. The root mean square of v_{diff},

$$v_{diff} = \overline{v}_s - \overline{v}_i \tag{19}$$

$$v_{rms} = \left[\frac{1}{N}\sum v_{diff}^2\right]^{\frac{1}{2}} \tag{20}$$

is 0.10 m/s, where N is the number comparisons.

[51] While the differences could result from measurement or technique errors, they could also represent real differences between the interior measured by the electromagnetic current meter and the surface currents estimated from the OCM. Four potential process-based sources of discrepancy were considered: vertical shear due to a bottom boundary layer; shear due to a surface roller stress; surface mass transport velocity; and shear due to surface wind forcing.

[52] A mean longshore current, flowing over the bottom, will develop a shear profile described by a logarithmic boundary layer [*Monin and Yaglom*, 1975], but the comparison data set containing a surface measurement and one in the interior cannot be used to test for a log layer. Previously measured vertical shear in the upper portion of the water column due to a bottom boundary layer has been observed to be about 0.1 m/s, [e.g., *Garcez Faria et al.*, 1998], while the magnitudes of the differences measured in this experiment were comparable, ranging from near zero to about 0.3 m/s with a root mean square value of 0.10 m/s. However, the sign of v_{diff} for a bottom boundary layer should be that of the interior flow, and our observations show differences of both signs (Figure 16) making boundary layer flow an unlikely cause of the observed discrepancies. Current meter misalignment (at worst 5°) and contamination of the alongshore current by undertow (at most 0.5 m/s) could cause the interior flow to be stronger than the surface, but we expect this to cause about 0.05 m/s of contamination, usually much less.

[53] The relationship of v_{diff} to alongshore directed roller stress was examined by calculating the alongshore component of roller stress [*Dally and Brown*, 1995] using the cross-sectional area representation of the roller by *Svendsen* [1984]

$$\tau^{y}_{roller} = \rho_r g 0.9 H_0^2 \sin(\beta_s)\sin(\alpha) \tag{21}$$

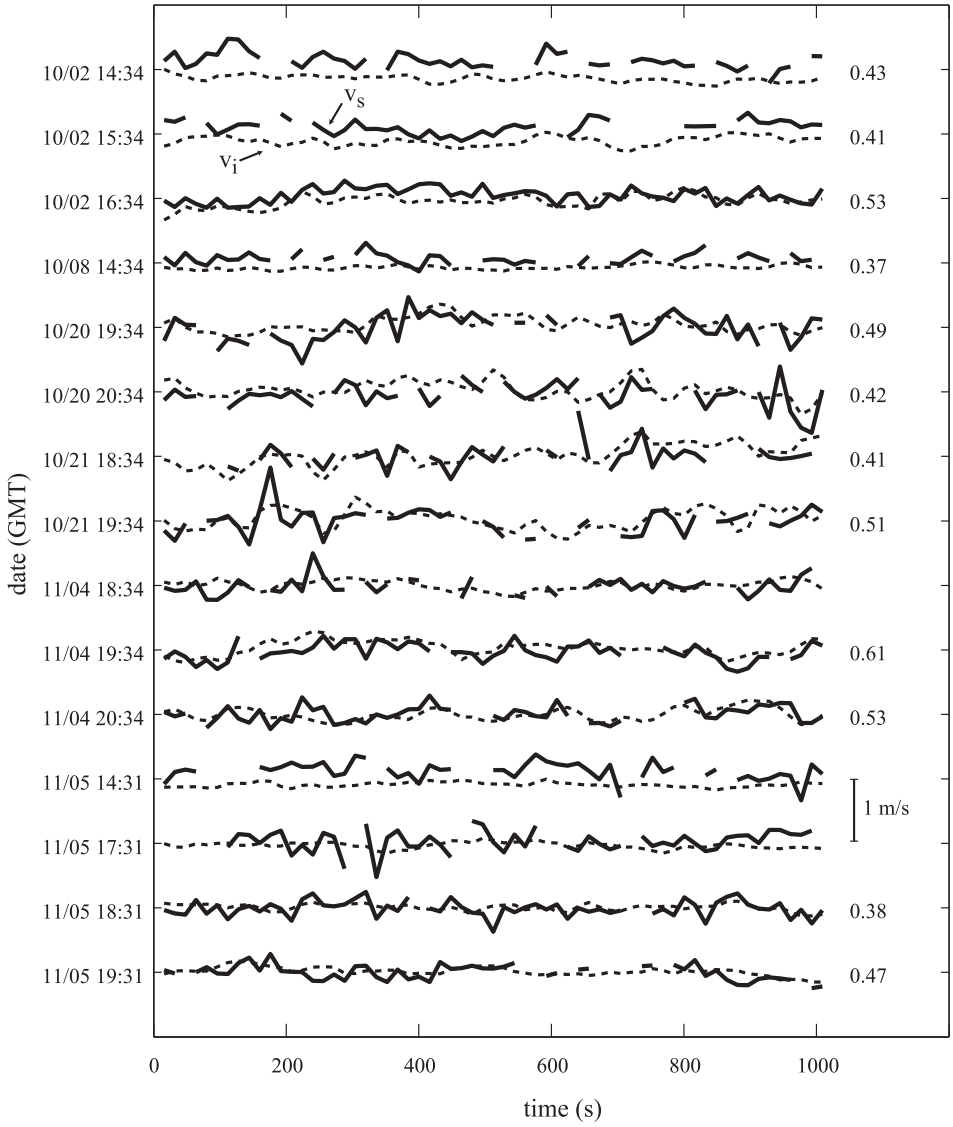

Figure 19. Fifteen sample surface (solid lines) and interior (dashed lines) longshore current time series. Only surface current data passing the criteria described in the text are plotted. The cross-correlation value computed for each time series pair is listed to the right; nonstatistically significant correlation values are omitted.

where ρ_r, the roller density, was taken as 100 kg/m^3, and H_0 is the significant wave height, or $4\sigma_\eta$. The results showed no significant relationship (r = 0.07) and are not shown, however our estimate of roller stress is very rough and a more focused experiment may provide a definitive answer.

[54] Lagrangian surface mass transport [*Dean and Dalrymple*, 1984], a result of linear wave theory using finite amplitude approximation, generates a mean surface flow in the direction of wave propagation. Waves approaching a beach obliquely will contribute an alongshore component of surface mass flux velocity, $\bar{v}_{smf}$. Assuming shallow water, the time averaged surface mass transport reduces to

$$\bar{v}_{smf} = \frac{E}{\rho h C}\sin(\alpha) \tag{22}$$

where E is the wave energy and ρ is the water density. Using linear wave theory and (22) we find the size of this term is small (< 8 cm/s) for the observed data. Compared to v_{diff}, surface mass flux velocity has no convincing relationship (r = 0.11) and is not shown.

[55] Shear due to a surface boundary layer could be driven by the alongshore component of wind stress. A plot of v_{diff} versus alongshore wind stress for the full data set shows a scattered relationship with a correlation of 0.50 (Figure 18). The scatter is decreased significantly and the correlation increased to 0.75 by removing observations for which the wind and waves were aligned to within ±45° (i.e., cases for which currents forced by winds and waves are not simply separable).

[56] We model the alongshore velocity difference Δv due to wind-induced surface boundary layer for cases when wind and waves were not aligned, as described above,

$$\Delta v = \frac{\tau^y_{wind}}{|\tau^y_{wind}|k}\sqrt{\frac{|\tau^y_{wind}|}{\rho}}\ln\left(\frac{d+z_0}{z_0}\right), \tag{23}$$

where ρ is the water density, d is the depth of the in situ instrument from mean sea level, $k = 0.4$ is von Karman's constant, and z_0 is an empirical parameter analogous to a roughness parameter. We used a representative z_0 (= 0.0034) as the median of the set of z_0 that solve equation (23) when v_{diff} is substituted for Δv. The modeled velocity offsets are well correlated with v_{diff} (r = 0.68). The RMS error for wind shear corrected currents using (23), for cases when waves and wind are not aligned, is 0.07 m/s compared to 0.09 m/s for uncorrected velocity estimates. While a slightly scattered relationship between v_{diff} and alongshore wind stress is observed, it appears that the data are consistent with a wind-induced surface velocity shear.

4.2. Time Series Sampling

[57] The OCM technique shows skill in estimating the mean alongshore current on the basis of 17-min data runs, and it is tempting to consider the degree to which time-varying signals can be resolved. Fifteen example time series of surface longshore currents, which retain at least 75% of the original (32 s) velocity estimates after the quality control procedures, are plotted in Figure 19 along with the corresponding in situ records. Zero time lag cross correlations, noted on the figure, show that all but three of the time series pairs are significantly correlated (a typical 95% significance level is 0.24, but varies with the number of OCM estimates in each time series). The records with lowest correlations were found to be associated with data runs with only weak in situ variability.

5. Discussion

[58] One attraction of the optical current meter technique was the lack of need for any in situ measurements or empirical calibration coefficients. However, the estimates can be clearly improved by accounting for misregistration effects (improvement in RMS error from 0.15 to 0.10 m/s) and for a surface wind stress (further reduction of RMS error to 0.06 m/s for cases of southerly wave approach). However, these corrections require estimation of additional in situ data (wave height, angle and period and wind stress). In cases where this information is available, corrections to the raw estimate are easily calculated. However, in the absence of such data, even approximations can yield improvements in OCM estimate quality. For the data set described above, the misregistration correction, $v_{apparent}$, had a mean of −0.12 m/s and a standard deviation of 0.05 m/s. From equation (12) it is clear that this value scales with longshore displacement between the camera and observation point, so that empirical mean correction could be easily found for other locations. It is also worth noting that to avoid having to make a correction for misregistration at all, the optimal arrangement is to position the OCM analysis pixel array directly offshore of the camera.

[59] The optical current meter offers a number of cost and logistic advantages. These include the ease of set up and deployment, the ability to change and adapt the placement of an optical current meter to changing conditions (e.g., a slowly evolving bathymetry or changing wave conditions), the ability to deploy multiple OCM arrays simultaneously in a variety of configurations, and the long term (Coastal Zone Management) measurement capability made possible from the long-lived camera stations on which the OCM relies.

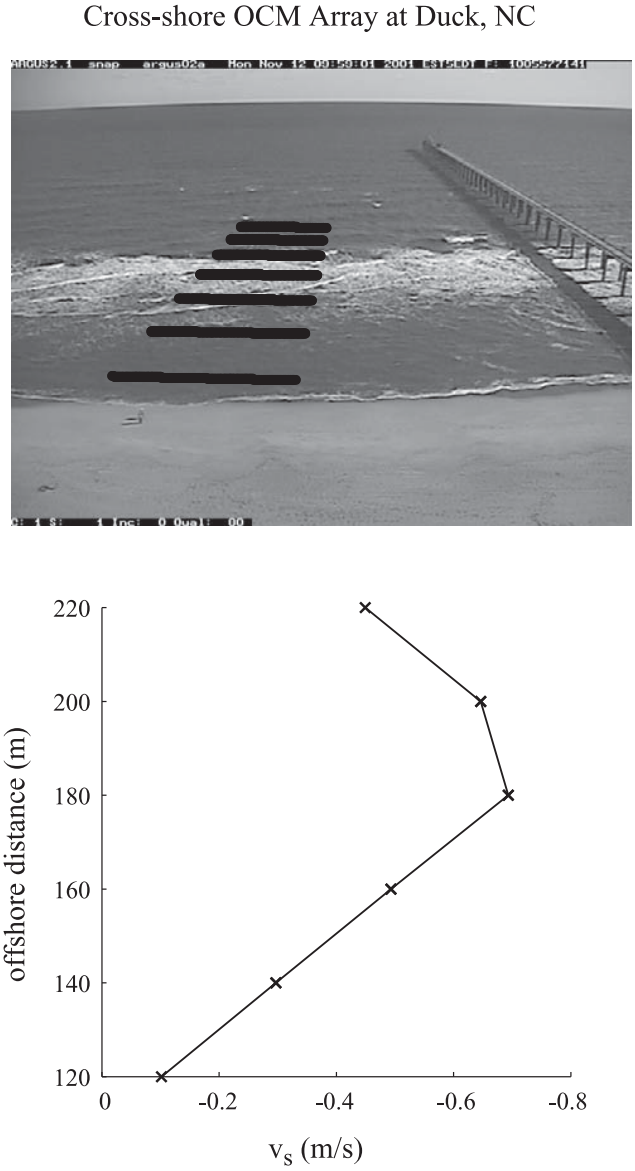

Figure 20. (top) A cross-shore OCM array designed to measure the mean cross-shore profile of the longshore current. (bottom) A 3-hour mean current profile showing a current peak in the surf zone at about the breakpoint.

[60] One application of the OCM might be to measure and monitor longshore currents to estimate alongshore sediment transport as a driving factor in sediment transport models. This will be important in applications such as predicting erosion and accretion rates of beach sediment, analyzing the impact of structures like jetties and piers on sediment transport, and in analyzing the flow field in the vicinity of beach nourishments and inlets. Figure 20 shows an example array that could be used to measure the cross-shore profile of the longshore current.

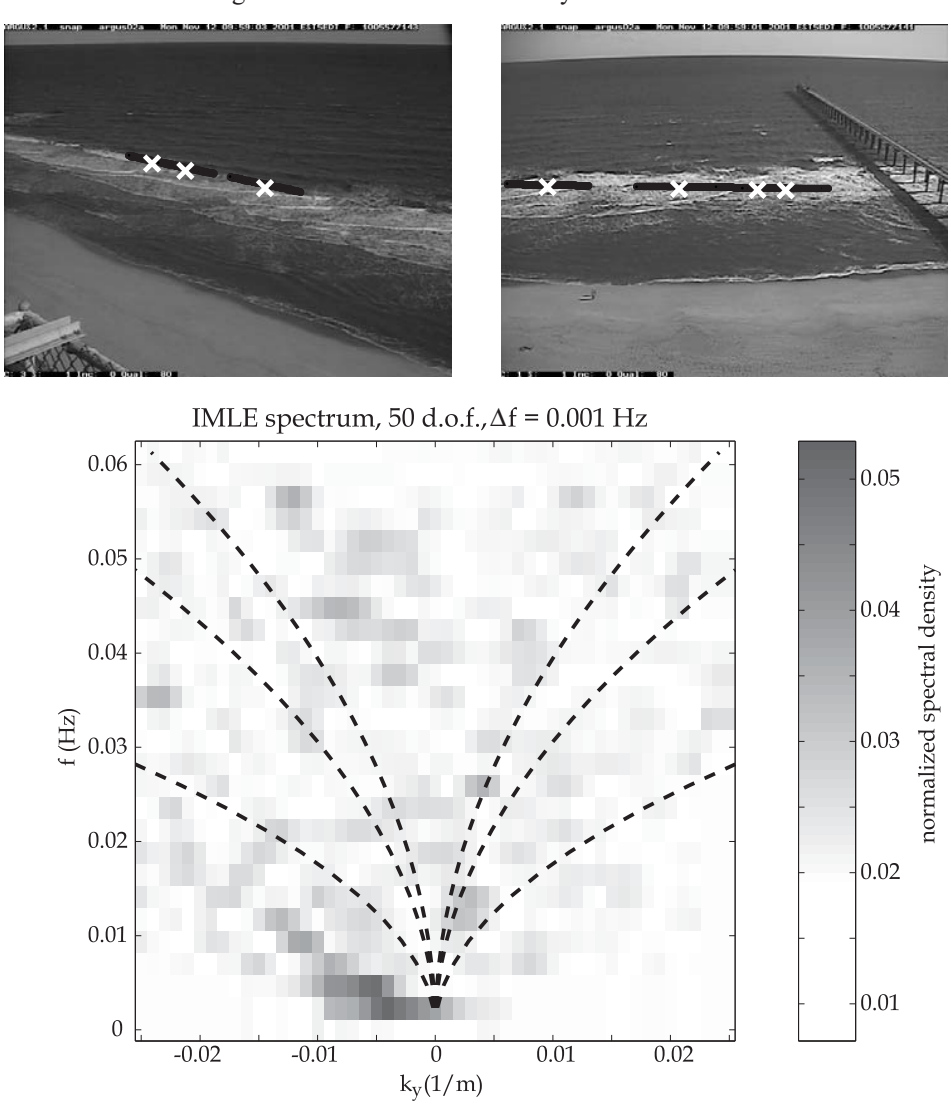

Figure 21. (bottom) IMLE spectrum produced from (top) 3-hour records of longshore current velocity from the shear wave array. Energy concentration in the lower frequencies may be associated with southward propagating shear waves. Also plotted are the estimated dispersion curves for 0, 1, and 2 mode edge waves.

The array consisted of 7 individual OCMs spaced 20 m apart and spanning 140 m across the surf zone, and revealed a sensible map of longshore current structure (Figure 20 (bottom)).

[61] Optical current meters may also be useful in studying shear waves, a recently discovered type of motion in the surf zone associated with longshore current instabilities [*Bowen and Holman*, 1989; *Oltman-Shay et al.*, 1989]. Shear waves were discovered from IMLE frequency-wave number spectral analysis [*Pawka*, 1983] of data from longshore-lagged arrays of electromagnetic current meters. To test this application, a similar longshore-lagged array of OCM's was sampled for a small number of 3-hour records at Duck, North Carolina, in November 2001 (Figure 21). The OCM measured surface currents were used to produce an IMLE frequency-wave number spectrum for one 3-hour collection, and although the spectrum is noisy because of the use of unedited raw OCM time series, a clear ridge of energy in the expected shear wave region of the spectrum is apparent (Figure 21 (bottom)). While no ground truth data were available to confirm the presence of shear waves a rough estimate of the total variance of the spectrum for the shear wave band (frequencies less than 0.001 Hz) was 0.04 m^2/s^2 (0.2 m/s standard deviation), a reasonable value comparable to previous shear wave measurement at Duck [*Oltman-Shay et al.*, 1989]. Moreover, the mean longshore current was observed to be $\sim$0.7 m/s and shear waves would be expected on the apparent barred profile. It seems likely that OCM techniques could contribute significantly

to shear wave studies by providing observations at different sites and under different conditions.

6. Conclusions

[62] A method has been developed to measure surface longshore current time series in the surf zone through optical imaging of the alongshore drift of persistent sea foam. In contrast to patch-based foam tracking techniques, this optical current meter uses time series data from only an alongshore oriented transect of pixels. The space-time data are Fourier transformed to a frequency-wave number spectrum, then transformed to a velocity spectrum, and, finally, fitted to a spectral model based on the advecting foam signature. The method yields 95% confidence limits on velocity estimates, and a measure of the quality of the input video data.

[63] Tests of the OCM, performed with synthetic data, indicate this method accurately estimates the mean current (maximum RMS error of 0.033 m/s) for a range of mean velocities (0 to 1.5 m/s) of contaminating wave motions (maximum longshore component of wave orbital velocities from 0 to 0.5 m/s) and analysis window lengths (8, 16, 32, 64 and 128 s). An optimal size window (32 s) was found to yield small errors (rms error = 0.012 m/s) while maintaining adequate temporal resolution of low-frequency motions, and is recommended for any further implementation of the OCM.

[64] A field test conducted with data from Duck, North Carolina, showed mean longshore surface currents measured with the OCM correspond closely to mean currents measured from a collocated in situ current meter (rms error of 0.15 m/s for the basic technique, reducing to 0.10 m/s when known misregistration errors were corrected). The gain between the two measurements was not statistically different from one. Differences between mean surface and interior currents could not be explained by shear due to the bottom boundary layer and were not correlated to a rough proxy of the alongshore component of wave roller stress. However, the differences were significantly correlated to the alongshore component of local wind stress ($r = 0.50$). This correlation was improved by considering cases when local winds did not reasonably contribute to the wave field ($r = 0.75$, for waves and wind not aligned within $\pm 45^\circ$). A dynamically based model of the surface wind-driven shear layer correlated well ($r = 0.68$) with the observed shear, again only for cases when waves and wind were not aligned. For cases when wind and waves are aligned the, the relative roles of wind stress, roller stress and boundary layer can often be confounded, and are not separable by correlation analysis.

[65] Ease of logistics and low cost should make the optical current meter technique valuable for both monitoring studies and processes investigations.

[66] **Acknowledgments.** The authors wish to thank Steve Elgar and Bob Guza for providing invaluable ground truth data including pressure sensor and longshore current time series, and John Stanley for continuous support for a variety of video, computing and life issues. Wind and wave climate and bathymetric data were provided by the hardworking staff of the FRF. We thank the Office of Naval Research Coastal Dynamics Program for support for this research (N00014-02-1-0154).

References

Bendat, J. S., and A. G. Piersol, *Random Data Analysis and Measurement Procedures*, 2nd ed., John Wiley, New York, 1986.

Birkemeier, W. A., H. C. Miller, S. D. Wilhelm, A. E. DeWall, and C. S. Gorbics, *A* User's guide to the Coastal Engineering Research Centers (CERC's) field research facility, *Misc. Rep. CERC-85-1*, U. S. Army Eng. Waterw. Exp. Stn., Vicksburg, Miss., 1985.

Birkemeier, W. A., C. E. Long, and K. K. Hathaway, DELILAH, DUCK94 & SandyDuck: Three nearshore field experiments, in *Coastal Engineering 1996: Proceedings of the Twenty-Fifth International Conference*, edited by B. L. edge, Am. Soc. of Civ. Eng., Reston, Va., 1996.

Bowen, A. J., The generation of longshore currents on a plane beach, *J. Mar. Res.*, *27*, 206–215, 1969a.

Bowen, A. J., Rip currents: 1. Theoretical investigations, *J. Geophys. Res.*, *74*, 5467–5478, 1969b.

Bowen, A. J., and R. A. Holman, Shear instabilities of the mean longshore current: 1. Theory, *J. Geophys. Res.*, *94*, 18,023–18,030, 1989.

Dally, W. R., and C. A. Brown, A modeling investigation of the breaking wave roller with application to cross-shore currents, *J. Geophys. Res.*, *100*, 24,873–24,883, 1995.

Dean, G. R., and R. A. Dalrymple, *Water Wave Mechanics for Engineers and Scientists*, Prentice-Hall, Englewood Cliffs, N. J., 1984.

Elgar, S., R. T. Guza, W. C. O'Reilly, B. Raubenheimer, and T. H. C. Herbers, Wave energy and direction observed near a pier, *J. Waterw. Port Coastal Ocean Eng.*, *127*, 2–6, 2001.

Feddersen, F., R. T. Guza, S. Elgar, and T. H. C. Herbers, Alongshore momentum balances in the nearshore, *J. Geophys. Res.*, *103*, 15,667–15,676, 1998.

Garcez Faria, A. F., E. B. Thornton, T. P. Stanton, C. V. Soares, and T. C. Lippmann, Vertical profiles of longshore currents and related bed shear stress and bottom roughness, *J. Geophys. Res.*, *103*, 3217–3232, 1998.

Guza, R. T., E. B. Thornton, and J. N. Christensen, Observations of steady longshore currents in the surf zone, *J. Phys. Oceanogr.*, *16*, 1959–1969, 1986.

Holland, K. T., and R. A. Holman, The statistical distribution of swash maxima on natural beaches, *J. Geophys. Res.*, *98*, 10,271–10,278, 1993.

Holland, K. T., R. A. Holman, T. C. Lippmann, J. Stanley, and N. Plant, Practical use of video imagery in nearshore oceanographic field studies, *IEEE J. Oceanic Eng.*, *22*, 81–92, 1997.

Holland, K. T., J. A. Puleo, and T. N. Kooney, Quantification of swash flows using video-based particle image velocimetry, *Coastal Eng.*, *44*, 65–77, 2001.

Holman, R. A., A. H. Sallenger Jr., T. C. Lippmann, and J. W. Haines, The application of video image processing to the study of nearshore processes, *Oceanography*, *6*, 78–85, 1993.

Jenkins, G. M., and D. G. Watts, *Spectral Analysis and its Applications*, Holden-Day, San Francisco, 1968.

Komar, P. D., *Beach Processes and Sedimentation, Second Edition*, Prentice-Hall, New Jersey, 1998.

Large, W. G., and S. Pond, Open ocean momentum flux measurements in moderate to strong winds, *J. Phys. Ocean.*, *11*, 324–336, 1981.

Lippmann, T. C., and R. A. Holman, Quantification of sand bar morphology: A video technique based on wave dissipation, *J. Geophys. Res.*, *94*(C1), 995–1011, 1989.

Lippmann, T. C., and R. A. Holman, The spatial and temporal variability of sand bar morphology, *J. Geophys. Res.*, *95*(C7), 11,575–11,590, 1990.

Lippmann, T. C., and R. A. Holman, Phase speed and angle of breaking waves measured with video techniques, paper presented at a Specialty Conference on Quantitative Approaches to Coastal Sediment Processes, Am. Soc. of Civ. Eng., Seattle, WA, 1991.

Long, C. E., and J. M. Oltman-Shay, Directional characteristics of waves in shallow water, *Tech. Rep. CERC-91-1*, U. S. Army Eng. Waterw. Exp. Stn., Vicksburg, Miss., 1991.

Longuet-Higgins, M., Longshore currents generated by obliquely incident sea waves, 1, *J. Geophys. Res.*, *75*(33), 6778–6789, 1970a.

Longuet-Higgins, M., Longshore currents generated by obliquely incident sea waves, 2, *J. Geophys. Res.*, *75*(33), 6790–6801, 1970b.

Monin, A. S., and A. M. Yaglom, *Statistical Fluid Mechanics: Mechanics of Turbulence*, vol. 2, MIT Press, Cambridge, 1975.

Munk, W. H., and M. A. Traylor, Refraction of ocean waves: A process linking underwater topography to beach erosion, *J. Geol.*, *55*, 1–26, 1947.

Oltman-Shay, J., P. A. Howd, and W. A. Birkemeier, Shear instabilities of the mean longshore current 2. field observations, *J. Geophys. Res.*, *94*(C12), 18,031–18,042, 1989.

Pawka, S. S., Island shadows in wave directional spectra, *J. Geophys. Res.*, *88*(C4), 2579–2591, 1983.

Plant, N. G., and R. A. Holman, Intertidal beach profile estimation using video images, *Mar. Geol.*, *140*, 1–24, 1997.

Press, H. W., S. A. Teukolsky, W. T. Vetterling, and B. P. Flannery, *Numerical Recipes in: The Art of Scientific Computing Second Edition*, Cambridge University Press, Cambridge, 1992.

Reniers, A., Longshore current dynamics, Ph.D. thesis, Delft Technical University, Delft, Netherlands, 1999.

Stockdon, H. F., and R. A. Holman, Estimation of wave phase speed and nearshore bathymetry from video imagery, *J. Geophys. Res.*, *105*(C9), 22,015–22,033, 2000.

Svendsen, I. A., Mass flux and undertow in a surf zone, *Coast. Eng.*, *10*, 347–365, 1984.

Taylor, G. I., Skin friction of the wind on the Earth's surface, *Proceedings of the Royal Society of London*, *92*(637), 196–199, 1916.

Wolf, P. R., and B. A. Dewitt, Elements of Photogrammetry: With Applications in GIS, McGraw-Hill, Boston, 2000.

C. C. Chickadel, M. H. Freilich, and R. A. Holman, College of Oceanic and Atmospheric Sciences, Oregon State University, Corvallis, OR 97331, USA. (cchickad@coas.oregonstate.edu)